Available online at www.sciencedirect.com
ScienceDirect
Trans. Nonferrous Met. Soc. China 35(2025) 405−417
Transactions of Nonferrous Metals Society of China
www.tnmsc.cn

Improving microstructure, tensile properties and corrosion resistance of AA6016 and AA2519 alloys friction stir lap joints via TIG arc

Tie YI[1,2,3], Sheng-dan LIU[1,2,3], Chen FANG[1,3], Geng-duo JIANG[4], Xuan-xuan DAI[1,3]

1. School of Materials Science and Engineering, Central South University, Changsha 410083, China;
2. National Key Laboratory of Science and Technology on High-strength Structural Materials, Central South University, Changsha 410083, China;
3. Key Laboratory of Non-ferrous Metals Materials Science and Engineering, Ministry of Education, Central South University, Changsha 410083, China;
4. School of Mechanical and Automotive Engineering, South China University of Technology, Guangzhou 510640, China

Received 23 June 2023; accepted 4 December 2023

Abstract: The effects of tungsten inert gas arc-assisted friction stir welding (TIG-FSW) on the microstructure, tensile properties and corrosion resistance of AA6016 and AA2519 alloys lap joints were investigated by means of optical microscope, scanning electron microscope, tensile test at room temperature, corrosion immersion tests and electrochemical measurements. The results show that the introduction of TIG arc during FSW process results in a more uniform microstructure of the joint with no tunnel hole defects. Furthermore, it enhances tensile strength and elongation of the joint with increased rates of 11.5% and 50.0%, respectively; meanwhile, the corrosion current density and largest corrosion depth are decreased with reduction rates of 78.2% and 45.7%, respectively. TIG-FSW can promote flow, contact and diffusion of materials, thus improving microstructure of the joint. Additionally, it reduces the size and number of secondary phase particles. Consequently, these factors contribute to the higher tensile properties and corrosion resistance of the joints.

Key words: friction stir welding; lap joint; dissimilar aluminum alloys; secondary phase particles; microstructure; tensile properties; corrosion resistance

1 Introduction

In industrial applications, the demand for friction stir welding (FSW) of dissimilar aluminum alloys has increased dramatically to achieve the structural light-weight and performance optimization. For instance, AA6xxx and AA2xxx alloys are often used in aerospace, transportation, and military structural parts [1,2]. In the welding of such dissimilar aluminum alloys, lap joints are one of the most common connection methods in panel structures, such as skin-stringer welded structures of aircraft fuselage [3]. However, the main problem for FSW of dissimilar aluminum alloys is the insufficient material flow, which results in nonuniform microstructure and hole defects in the nugget zone (NZ), and decreases the joint properties [4−7]. For instance, LI et al [6] studied the microstructures of the FSW joints of AA6061 and AA2024 alloys and found that insufficient solid-state flow during FSW can produce significant tunnel defects, resulting in reduced joint strength. BRAUN et al [7] studied the corrosion behavior of

Corresponding author: Sheng-dan LIU, Tel: +86-731-88830265, E-mail: lsd_csu@csu.edu.cn
DOI: https://doi.org/10.1016/S1003-6326(24)66688-4

the friction stir welded joints of AA6056 and AA2024 alloys and found that the microstructural changes of the dissimilar aluminum alloy joints caused by the welding process lead to galvanic coupling, which accelerates the corrosion of AA6056 alloy in the NZ. Therefore, it is essential to enhance the material flow during FSW to improve properties of dissimilar aluminum alloy joints.

It is believed that different plasticities of dissimilar aluminum alloys and insufficient welding heat input during FSW are the main reasons for the uneven mixing of materials [8−10]. For instance, LI et al [9] studied the solid-state flow visualization in the FSW joints of AA6061 and AA2024 alloys and found that different plasticities of these alloys lead to the formation of complex vortex, whorl, and swirl features in the NZ. MURR et al [10] studied the intercalation vortices and related microstructural features of FSW joints of AA6061 and AA2024 alloys and found that the microstructures of the NZ resemble turbulent vortex. At present, the plastic flow of the material is often enhanced by optimizing the welding parameters and the structure of stir tool, so as to improve the microstructure of the NZ and the properties of the joint [11−13]. For instance, OUYANG and KOVACEVIC [12] studied the effect of processing parameters on the material flow and microstructure of friction stir welded joint of AA6061 and AA2024 alloys and found that increasing the rotational speed results in more uniform mechanical mixing of material in the dissimilar joint, and consequently, the hardness is more uniform in the joint. This is because the higher rotational speed provides more momentum for the return flow of material, allowing it to spread more widely and mix more evenly across the joint. IZADI et al [13] studied the effect of tool geometry on material flow during FSW of AA6061 and AA2024 alloys and found that the use of a threaded pin leads to increased material mixing at lower traverse speeds, while the use of a smooth pin does not result in better mixing. However, improving the plastic flow of materials through the optimization of welding parameters and stir tool structure requires extensive experimental work, and achieving a high level of reproducibility can be challenging [14].

Recently, tungsten inert gas arc-assisted FSW (TIG-FSW) has been found to effectively improve the plastic flow of materials during the welding process [15−19]. For instance, BANG et al [17] studied the formability of TIG arc-assisted AA6061 alloy and STS304 stainless steel FSW joints, and found that TIG arc can preheat the steel surface, enhance the plastic flow of the material, and promote the diffusion and bonding between dissimilar materials. XU et al [18] studied the microstructure of the FSW joint interface between AA2024 alloy and Q235 steel assisted by TIG arc, and found that TIG arc can significantly improve the material flow, and therefore enhance the metallurgical bonding of the joint. YI et al [19] studied the microstructure of the TIG-FSW joint of AA2519 alloy and found that TIG arc improves the material flow, and therefore eliminates the hole defects in the joint. Therefore, it may be an effective way to solve the above problems for FSW of dissimilar aluminum alloys.

In this work, an FSW process assisted by TIG arc was reported to improve both tensile properties and corrosion resistance of the AA6016 and AA2519 alloys joint, and the mechanism was discussed based on microstructure examination. This helps to better understand the role of TIG in FSW process and expand the industrial application of dissimilar aluminum alloy lap joints.

2 Experimental

An AA6016 alloy sheet with a thickness of 0.8 mm was placed on an AA2519 alloy sheet with a thickness of 2.0 mm for lap welding, and the chemical compositions and tensile properties are listed in Table 1. During the conventional FSW (C-FSW), the inclination angle of the rotation axis

Table 1 Chemical compositions and tensile properties of AA6016 and AA2519 alloys

Alloy	Chemical composition/wt.%								Tensile property		
	Cu	Mn	Mg	Ti	Zr	Fe	Si	Al	R_m/MPa	$R_{p0.2}$/MPa	A/%
AA6016	0.20	0.20	0.40	0.15	−	0.50	1.25	Bal.	227	124	25.0
AA2519	5.80	0.30	0.20	0.05	0.02	0.10	0.02	Bal.	393	295	10.5

R_m, $R_{p0.2}$ and A are tensile strength, yield strength and elongation, respectively

and the press amount of the stir tool were 2.5° and 0.5 mm, respectively; the weldment was preheated to 75 °C without causing grain coarsening of the base metal (BM); the rotational speed was 1600 r/min, and the welding rate was 80 mm/min. The welding parameters of TIG-FSW were the same as those of C-FSW, but TIG arc (8 A) was used to produce high temperature and cathodic atomization in front of the stir tool, and an argon cover (10 L/min) was used to protect the weldment behind TIG arc. The detailed TIG-FSW process can be found in Ref. [19]. The weldments were cooled in the air to room temperature after welding.

The tensile properties of the joints were tested on an MTS Landmark 370 testing machine at room temperature and three tensile specimens were tested to obtain an average value. The fracture surfaces of the joints after the tensile test were examined by a Zeiss MA 10 scanning electron microscope (SEM) with an energy dispersive X-ray spectroscopy (EDS). Cross-section specimens of the joints were mechanically polished, and corroded in 30% NaOH solution first for about 60 s, and then in 3% HNO_3 solution to remove the black corrosion products on the surface, cleaned in water, and finally dried to examine the fracture path and morphology by using a Leica DM2700M optical microscope.

The corrosive immersion test was performed according to ASTM G34—2001 and the specimen size was 50 mm × 20 mm × 2.8 mm. The joint surface was tested and the other five surfaces were sealed with sealant. The specimens were immersed in a solution of 234 g NaCl + 50 g KNO_3 + 6.3 mL HNO_3 diluted to 1 L with deionized water for 96 h, and the temperature was (25±3) °C controlled in a water bath. The standard three-electrode system was adopted for the electrochemical test performed on a Metrohm Multi AUTOLAB M204 instrument. The working electrode was the surface of the NZ with an area of 1 cm^2. The scanning range of the potentiodynamic polarization test was from −1.2 to −0.2 V, and the scanning speed was 1 mV/s. All electrochemical tests were carried out in a 3.5 wt.% NaCl solution at room temperature.

3 Results and discussion

3.1 Microstructure

The microstructure of the cross-section of the NZ in the two joints is shown in Fig. 1, and the white and dark gray zones are AA6016 and AA2519 alloys, respectively. In the NZ of the C-FSW joint, a large amount of AA6016 alloy flowed down from the upper part and inter-penetrated with AA2519 alloy, forming an inlaid morphology (Fig. 1(a), blue dotted frame); meanwhile, on the retreating side (RS), a large amount of AA2519 alloy flowed up to the surface (Fig. 1(a), Zones I, II and III). The area of the NZ is (12.53±0.32) mm^2. Moreover, there are tunnel hole defects and kissing bonds in the joint (Fig. 1(a)), and some scattered oxides are present in the kissing bonds, as shown in Fig. 2. These oxides are primarily attributable to the original oxide film present on the surface of aluminum alloys and the oxides produced at high welding temperatures [20]. Near the NZ surface, there are some elongated secondary phase particles in AA6016 alloy, as seen in Fig. 1(a_4), and their length, width and area fraction are (4.35±2.06) μm, (0.87±0.29) μm and (0.74±0.05)%, respectively. The EDS analysis showed that the composition of these particles is (81.3±3.11) at.% for Al, (7.79±0.39) at.% for Fe, (10.29±0.80) at.% for Si and (0.53±0.07) at.% for Mn, and they are likely Al(Fe,Mn)Si particles [21]. It is worth noting that there are a large number of secondary phase particles (Fig. 1(a_2)) with an area fraction of (10.19±1.06)% in AA2519 alloy. The EDS analysis showed that the composition of these particles is (67.88±6.23) at.% for Al, and (32.12±2.55) at.% for Cu, presumed to be Al_2Cu particles [22]. Moreover, in the border region between AA6016 and AA2519 alloys (Figs. 1(a_1) and (a_3)), there are a small number of Al(Fe,Mn)Si particles distributed on the side of AA6016 alloy. While on the side of AA2519 alloy, there are a large number of Al_2Cu particles.

While in the NZ of the TIG-FSW joint, the upper part of AA6016 alloy flowed down in a slender and streamlined shape, resulting in a compacted bonding, and there are no tunnel hole defects (Fig. 1(b)). The lower part of AA2519 alloy did not flow upward to the joint surface, but backfilled horizontally from the RS to the AS, and therefore the surface material is AA6016 alloy (Fig. 1(b)). The NZ area is (14.67±0.27) mm^2. Near the NZ surface (Figs. 1(b_1−b_4)), the length, width and area fraction of Al(Fe,Mn)Si particles are (2.07±0.86) μm, (0.58±0.21) μm and (0.22±0.01)%, respectively, significantly smaller than those of the

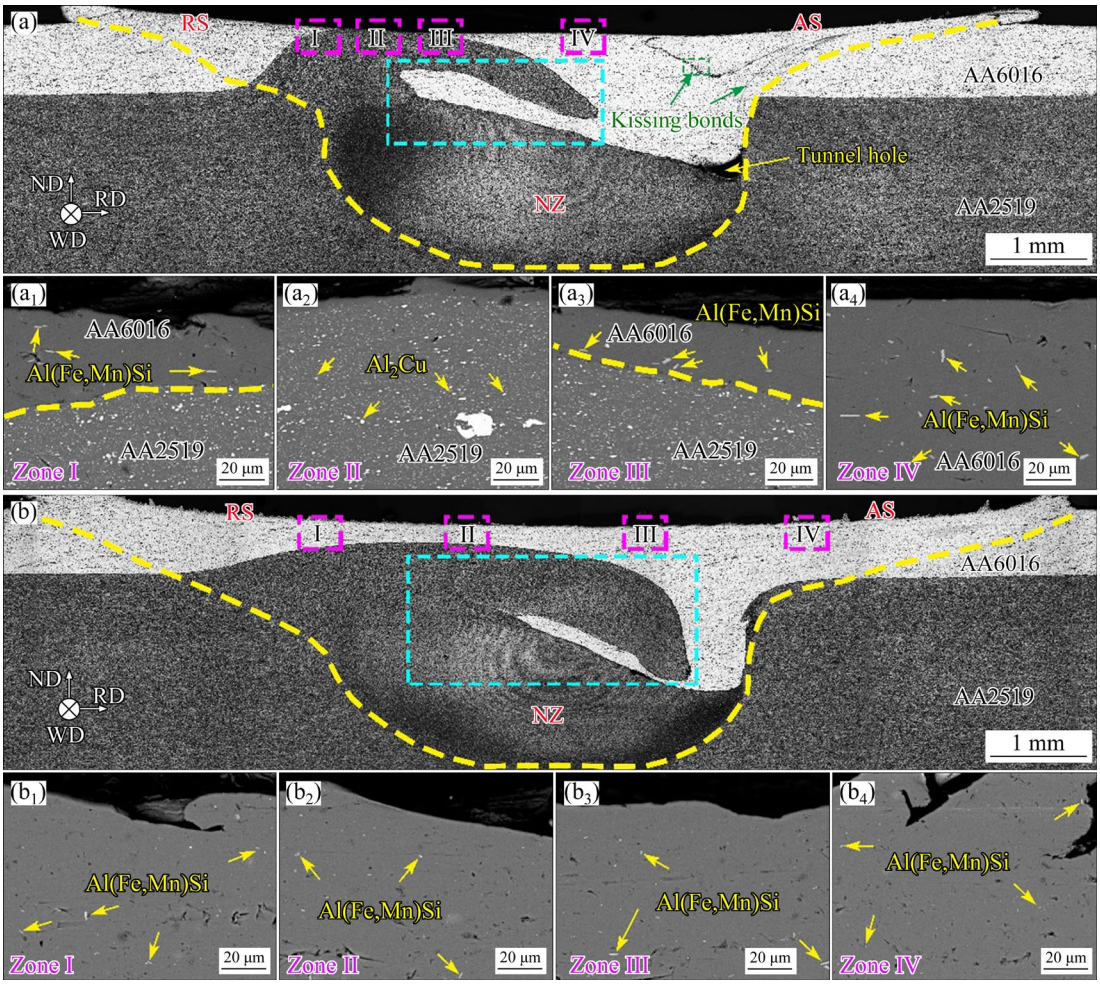

Fig. 1 Microstructures on cross-section of NZ in C-FSW (a, a_1−a_4) and TIG-FSW (b, b_1−b_4) joints obtained by SEM (ND and RD are the normal and rolling directions of the sheet, respectively; WD is the welding direction)

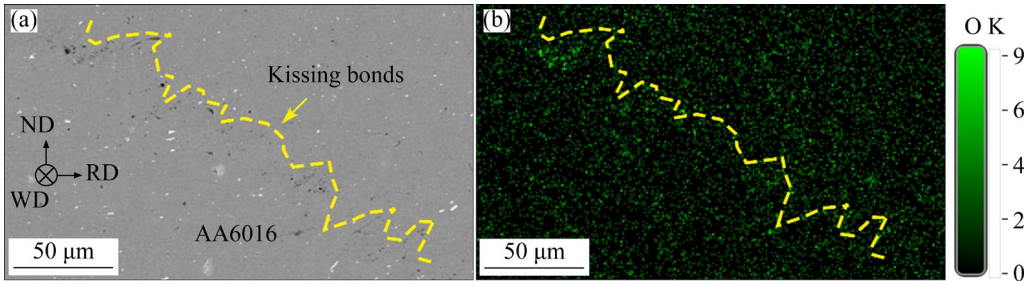

Fig. 2 SEM image of kissing bonds (a) and EDS mapping of oxygen (b) from green dotted frame in Fig. 1(a)

NZ in the C-FSW joint, and the decreased rates are about 52.4%, 33.3% and 70.3%, respectively. This is because TIG arc with 3500 K can melt the initial secondary phase particles and the Al matrix on the surface [23]. Then, the molten metal was rapidly cooled and solidified, the solute atoms were precipitated to form fine and discontinuous eutectic particles, and therefore the number of coarse secondary phase particles in the BM was drastically reduced. During the subsequent FSW, most of the fine eutectic particles were dissolved into the Al matrix, resulting in a high supersaturation of the solid solution. As a result, a large number of new fine secondary phase particles were formed during the subsequent cooling [24].

3.2 Tensile properties and fractograph

The engineering stress−strain curves of tensile specimens at room temperature are shown in Fig. 3. After the introduction of TIG arc, the strength of the

joints is increased from (208±1) to (232±3) MPa with an increased rate of 11.5%; meanwhile, the elongation is increased from (3.2±0.1)% to (4.8±0.3)% with an increased rate of 50.0%.

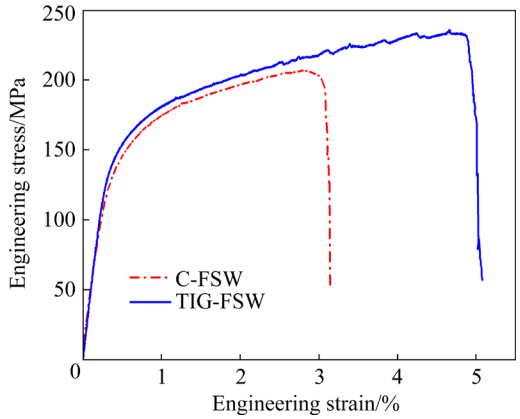

Fig. 3 Engineering stress−strain curves of tensile specimens at room temperature

The optical images showing fracture features of the joints after tensile testing are given in Fig. 4. The fracture path is zigzag in the C-FSW and TIG-FSW joints. In the C-FSW joint, the crack preferentially initiated at the tunnel hole defects and expanded upward and downward along 45° direction to the tensile direction (Fig. 4(a)). While in the TIG-FSW joint, there are no hole defects and kissing bonds, but from the tear marks at the intersection of AA6016 and AA2159 alloys on the AS of the NZ, it can be determined that the crack preferentially initiated here and propagated upward and downward (Fig. 4(b)). This is because the intersection of materials is often considered to be a critical weak region in the dissimilar aluminum alloy joints [25]. In order to better understand the fracture behavior, the fracture surfaces were examined by SEM, and some typical images are given in Fig. 5, which were taken from the positions indicated by green dotted frames in Fig. 4. Smooth cleavage surfaces with many large and shallow dimples and shear fracture marks (Fig. 5(b)) can be observed and the stress concentration is most likely to form at these locations [26,27] and thus the crack first starts in Zone II in Fig. 4(a). There are some continuous crack lines and cambium lamellar areas in Zone I in Fig. 4(a), as seen in Fig. 5(a), which exhibit poor mechanical bonding. This is because the stress tends to concentrate in the weak bonding region like kissing bonds [28], leading to local deformation and premature fracture. It can be seen from Fig. 5(c) that, there are many large deep dimples and some residual phases in Zone III, and the tearing edge is visible; these are typical features of transgranular fracture, indicating that significant plastic deformation occurred here during tensile process. It is because with the increase of strain, dislocations tend to accumulate in the softened zone [29], i.e., the bottom of the NZ. In conclusion, in the C-FSW joint, AA6016 alloy side exhibits a brittle fracture mode, while AA2519 alloy side exhibits a ductile fracture mode. Moreover, during tensile testing of this joint, the crack preferentially initiated at the tunnel hole defects, and then extended to the top and bottom of the joint, respectively; finally, the fracture path shown in Fig. 4(a) can be observed.

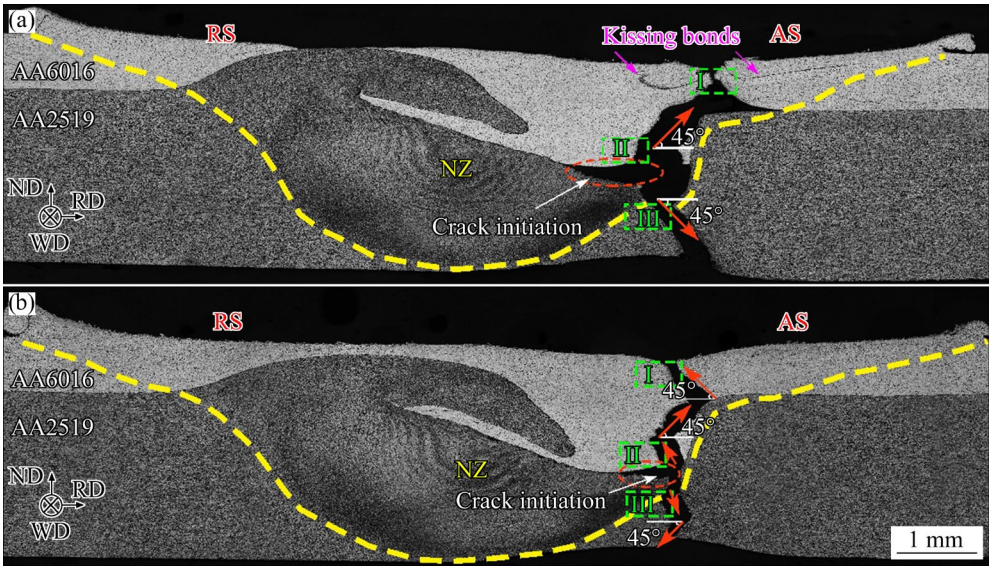

Fig. 4 Optical images showing fracture path in C-FSW (a) and TIG-FSW (b) joints after tensile testing

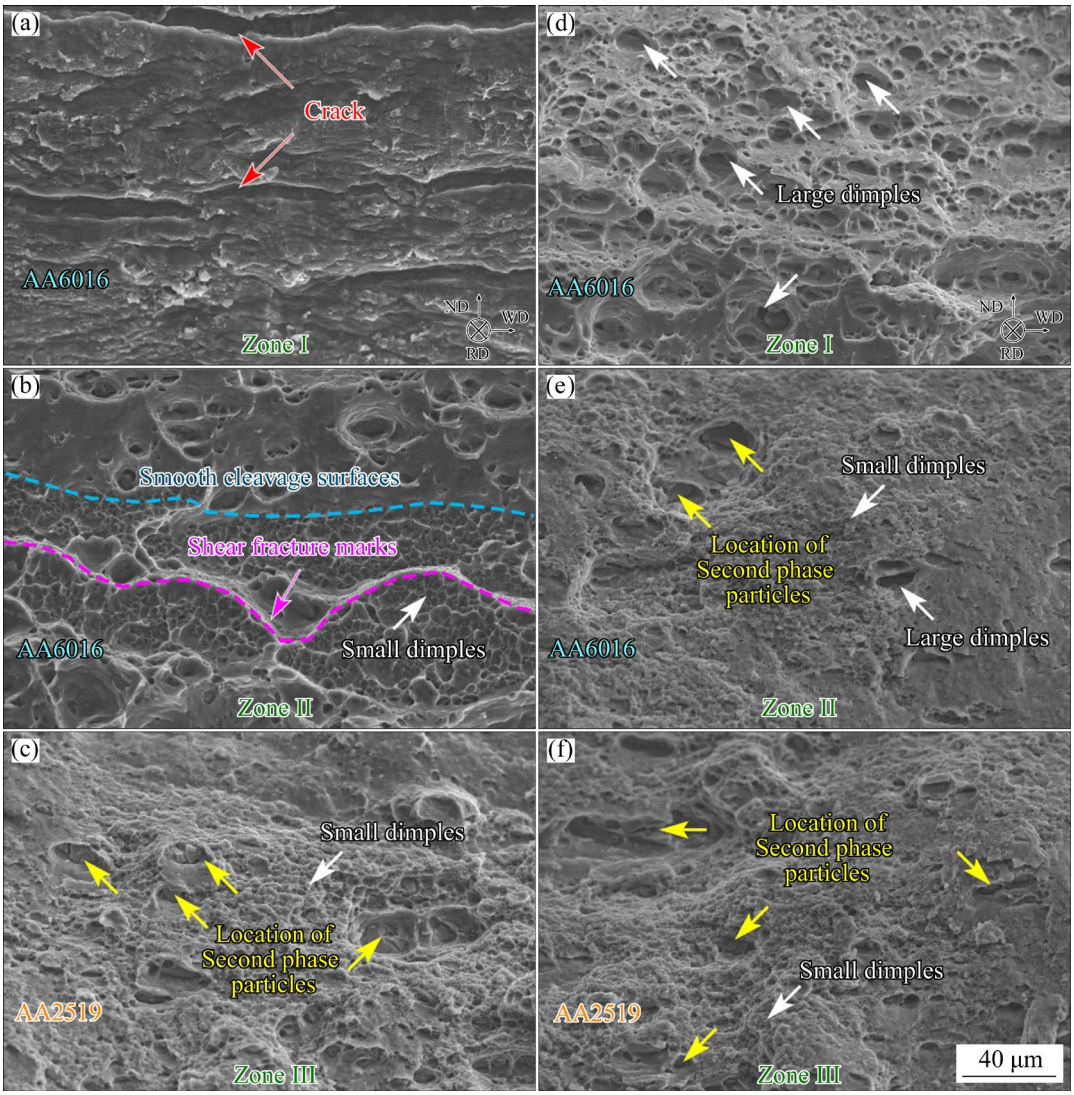

Fig. 5 SEM images of fracture surfaces of C-FSW (a−c) and TIG-FSW (d−f) joints: (a−c) From Zones I, II and III in Fig. 4(a), respectively; (d−f) From Zones I, II and III in Fig. 4(b), respectively

While in the TIG-FSW joint, there are some large deep dimples and residual phases in Zone II in Fig. 4(b), as seen in Fig. 5(e), and these are the characteristics of transgranular fracture, indicating that plastic deformation occurred in this zone. It is noteworthy that the fracture feature in Zone I of the TIG-FSW joint significantly differs from that of the C-FSW joint, as seen in Figs. 5(a) and (d). This zone exhibits multiple dimples of different depths, indicating a strong metallurgical bonding. However, the fracture features observed in Zone III of the TIG-FSW joint are similar to those of the C-FSW joint (Figs. 5(c) and (f)). Consequently, in the TIG-FSW joint, both AA6016 and AA2519 alloys sides exhibit a ductile fracture mode, which is consistent with the higher elongation.

3.3 Corrosion behavior

Figure 6 shows the corrosion features of the cross-section in the NZ of the two joints immersed in the corrosive solution for 96 h. As seen from Figs. 6(a, a_1−a_6), in the NZ of C-FSW joint, there are pitting corrosion and intergranular corrosion on AA6016 alloy side, and the largest depths of pitting corrosion and intergranular corrosion are 29.6 and 35.7 μm, respectively. However, on AA2519 alloy side, no obvious corrosion occurs, as see in Fig. 6(a_3). While for the TIG-FSW joint, as seen from Figs. 6(b, b_1−b_6), there are slight pitting corrosion and no intergranular corrosion in the NZ. The largest depth of pits is 19.4 μm, significantly smaller than that of the NZ in the C-FSW joint, and the decreased rate is 45.7%.

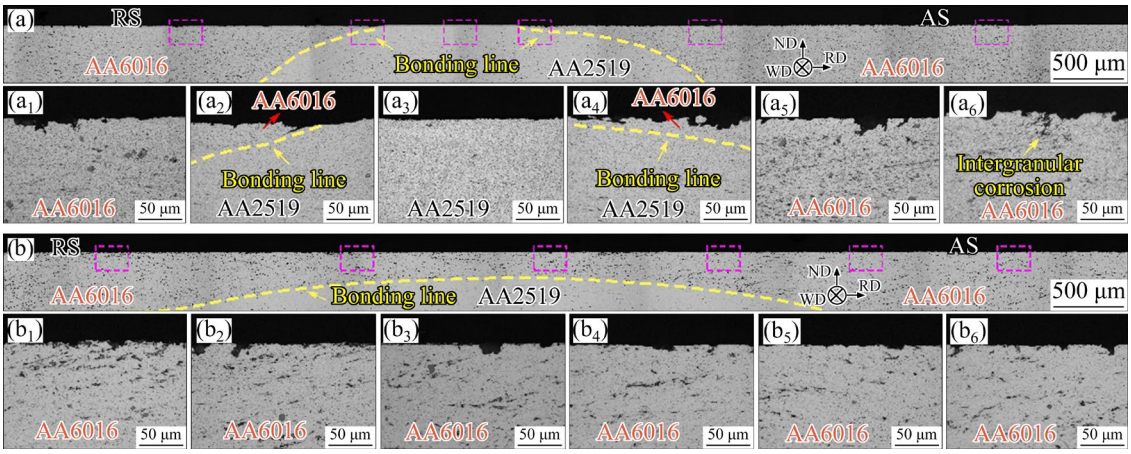

Fig. 6 Corrosion feature images of cross-section in NZ of C-FSW (a, a_1−a_6) and TIG-FSW (b, b_1−b_6) joints

3.4 Potentiodynamic polarization

In electrochemical reactions, the corrosion resistance of the material can be determined by its corrosion current density (J_{corr}) and the self-corrosion potential (φ_{corr}). Figure 7 shows the potentiodynamic polarization of BM and NZ in the two joints, and the electrochemical parameters are listed in Table 2. The φ_{corr} and J_{corr} values of AA2519 alloy are −0.623 V and 2.459 μA/cm^2, respectively, and larger than those of −0.732 V and 0.817 μA/cm^2 for AA6016 alloy. A higher J_{corr} indicates higher corrosion resistance, and the φ_{corr} reflects the corrosion tendency of the material [30,31]. It can be inferred that the corrosion resistance of AA6016 alloy is superior to that of AA2519 alloy. However, it should be noted that in the case of coupling AA6016 and AA2519 alloys together, AA2519 alloy becomes the cathode, whereas AA6016 alloy becomes the anode. As a result, anodic dissolution of AA6016 alloy occurred during immersion, as shown in Fig. 6(a).

After the introduction of TIG arc, the J_{corr} value is decreased from 5.777 to 1.257 μA/cm^2 with a decreased rate of 78.2%; meanwhile, the φ_{corr} value is decreased from −0.694 to −0.707 V with a decreased rate of 1.8%. This is because the uniform surface material of the NZ and a more dispersed distribution of finer secondary phase particles in the TIG-FSW joint (Fig. 1) weaken the galvanic corrosion, and decrease the J_{corr} value [32,33]. However, the NZ surface in the C-FSW joint contains part of AA2519 alloy (purple dotted frame in Fig. 1(a)) with higher potential (Table 2), leading to higher value of φ_{corr} [34]. Therefore, the NZ in

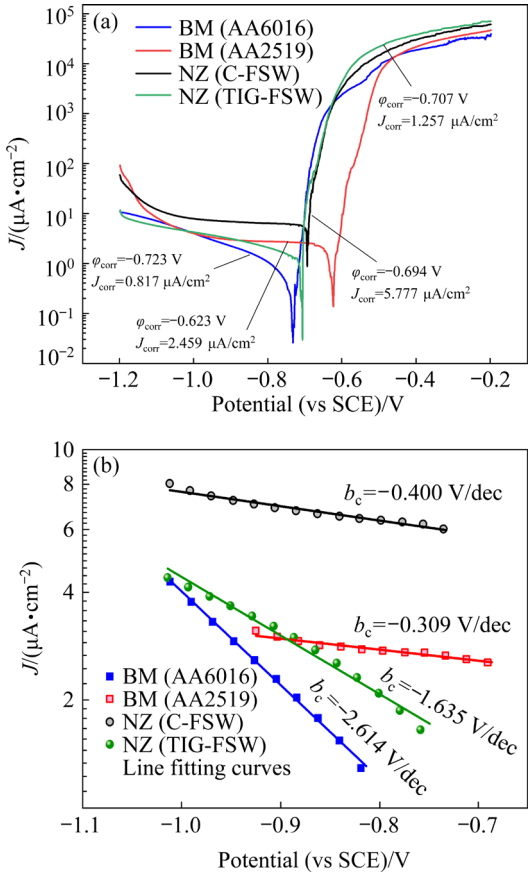

Fig. 7 Polarization curves of different samples in 3.5 wt.% NaCl solution: (a) Polarization curves; (b) Tafel lines

Table 2 Electrochemical parameters obtained by Tafel linear extrapolation

Specimen	φ_{corr}(vs SCE)/V	J_{corr}/(μA·cm^{-2})	b_c/(V·dec)
BM (AA2519)	−0.623	2.459	−0.309
BM (AA6016)	−0.732	0.817	−2.614
NZ (C-FSW)	−0.694	5.777	−0.400
NZ (TIG-FSW)	−0.707	1.257	−1.635

b_c: Cathode Tafel slope

the TIG-FSW joint with a lower J_{corr} value is expected to have higher corrosion resistance as confirmed by Fig. 7.

4 Discussion

Based on the above results, the enhancement of the tensile properties and corrosion resistance in the AA6016 and AA2519 alloys lap joint is closely related to the improved microstructure of the joint, and this is definitely due to the improved material flow during welding assisted by TIG arc, as described schematically in Fig. 8.

During the C-FSW process, the surface material flows from the front to the back of the stir pin and moves downward under the action of the stir tool, and therefore fills the instantaneous cavity behind the stir pin on the advancing side (RS), as described schematically in Fig. 8(a). Insufficient heat generation can lead to insufficient material flow, resulting in tunnel hole defects [35−37] (Fig. 1(a)). Meanwhile, part of the lower material flows upwards to fill the material void on the NZ surface (the purple dotted frame in Fig. 8(b)), resulting in nonuniform material distribution on the NZ surface. Moreover, the internal oxides in the NZ originate mainly from the oxide film present on the initial weldment surface and the oxidation products of the aluminum alloy formed during high temperature welding. As the oxides break down, they experience a periodic spiral flow along the stir pin, accumulate on the AS of the NZ, and form continuous oxide particles known as kissing bonds [38]. The kissing bonds are considered to be a weak bonding defect in the FSW joint [39].

While during the TIG-FSW process, the high temperature of TIG arc significantly reduces the deformation resistance of the material, promotes the flow of the surface material around the stir pin, and results in smaller instantaneous cavity compared with C-FSW, as described schematically in Figs. 8(a) and (c). It is beneficial to reducing the loss of the upper material and inhibiting the upward filling of the lower material, leading to the presence of AA6016 alloy in the surface layer (Fig. 1(b)). Moreover, the additional heat source promotes the contact and diffusion of the upper and lower materials in the NZ, and thus results in the elimination of tunnel hole defects and the formation of slender and streamlined shapes on the AS of the NZ (Fig. 1(b)), as described schematically in Fig. 8(d). Furthermore, previous work [19] showed that TIG-FSW can effectively clean the oxide film on the weldment surface by the cathodic cleaning effect of TIG arc, reduce the content of oxides inside the joint, and therefore eliminate the kissing bonds. As a result, premature failure was observed in the C-FSW joint with tunnel hole defects rather than in the TIG-FSW joint without defects during tensile testing (Figs. 3 and 4). In addition, the features of kissing bonds can affect the crack propagation, since cracks rapidly extend through weak bonding, leading to a decrease in tensile properties. Therefore, in the TIG-FSW joint without kissing bonds, rapid crack expansion is prevented, and higher tensile properties are obtained.

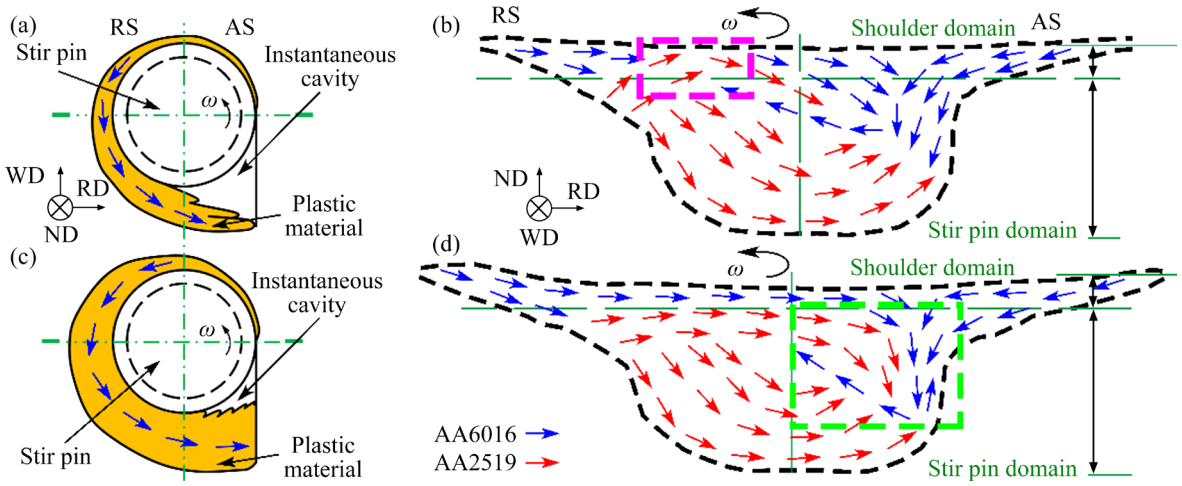

Fig. 8 Schematic diagrams of plastic flow in NZ during C-FSW (a, b) and TIG-FSW (c, d) processes: (a, c) NZ surface; (b, d) NZ cross-section

It can be seen from the above results that after the introduction of TIG arc, the corrosion resistance of the NZ is improved. To better understand the mechanism, the corrosion behavior on cross-section in the NZ of the two joints is compared and described schematically in Figs. 9 and 10, respectively. The corrosion behavior of the NZ in the C-FSW joint is shown in Fig. 9(a). Due to the self-corrosion potential difference between AA6016 and AA2519 alloys (Fig. 7(a)), AA6016 alloy is preferentially dissolved as an anode [40]. At the local position with high activity (such as the interface of dissimilar aluminum alloys), the large difference in corrosion potential (Fig. 9(b)) results in severe macro-galvanic corrosion on AA6016 alloy side. The anodic reaction is as follows:

$$Al=Al^{3+}+3e \quad (1)$$

$$2Al+6H^{+}+4Cl^{-}=2AlCl_2^{+}+3H_2\uparrow \quad (2)$$

$$Al^{3+}+H_2O+Cl^{-}=AlOHCl^{+}+H^{+} \quad (3)$$

$$Al^{3+}+3OH^{-}=Al(OH)_3\downarrow \quad (4)$$

On AA2519 alloy side, the cathodic reaction involves the reduction of water and oxygen:

$$2H_2O+O_2+4e=4OH^{-} \quad (5)$$

As described schematically in Fig. 9(a), the exposed surface of Al undergoes rapid ionization (Reaction (1)), resulting in an increase in the concentration of Al^{3+} in the intense corrosion zone and Cl^{-} continuously migrating into the zone, and this increases the concentration of Cl^{-}. Meanwhile, the pH value decreases and the H^{+} concentration increases in the zone, leading to acidification of the solution in the zone. The H^{+} produced by hydrolysis (Reaction (3)), along with Cl^{-}, promotes the continuous dissolution of Al in the zone (Reaction (2)). The oxygen cathodic reduction occurs on AA2519 alloy side (Reaction (5)) and generates OH^{-}. Then, the OH^{-} and Al^{3+} accumulate in the intense corrosion zone (Reaction (4)) and form the corrosion products $Al(OH)_3$. They hinder the exchange of medium inside and outside the zone, resulting in the formation of a blocked battery [41]. This forms an autocatalytic reaction that drives corrosion development and leads to the formation of severe corrosion. Furthermore, AA6016 alloy side far away from the interface experiences less macro-galvanic corrosion due to the reduced potential difference. Instead, the corrosion reaction primarily occurs through micro-galvanic corrosion between the secondary phase particles and the Al matrix, leading to the formation of pitting corrosion. As a result, the potential difference in the interfacial

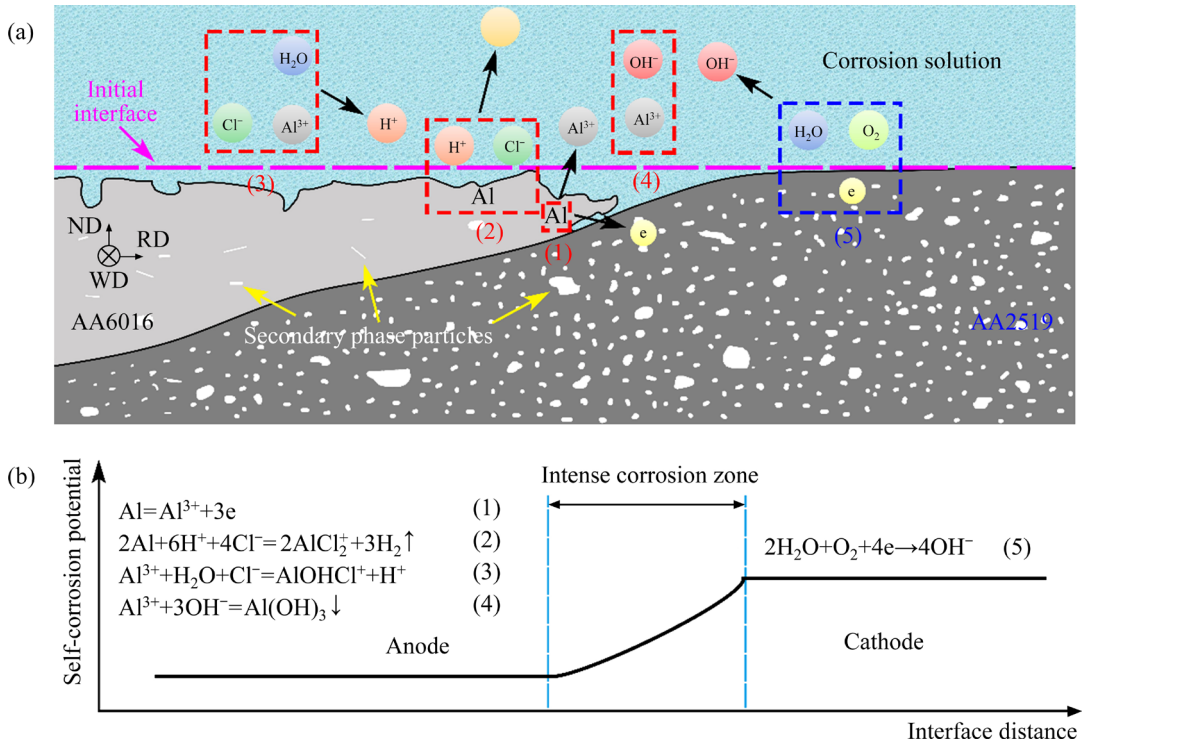

Fig. 9 Schematic diagram of corrosion behavior of NZ in C-FSW joint under macro-galvanic corrosion condition (a), and self-corrosion potential curve versus interface distance (b)

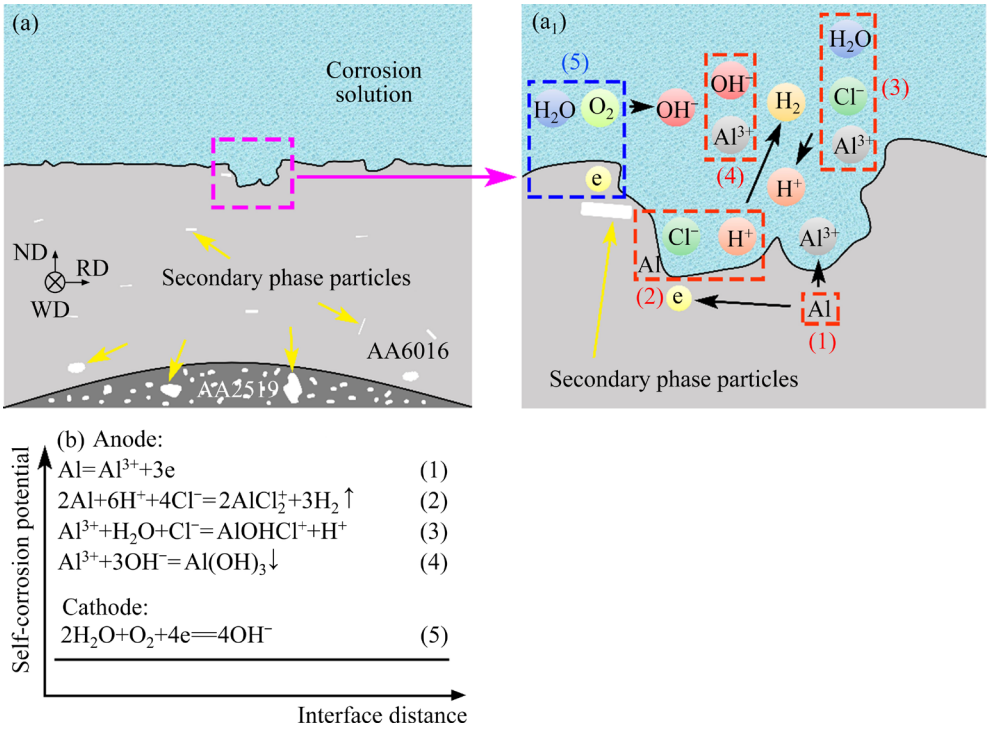

Fig. 10 Schematic diagrams of corrosion behavior of NZ in TIG-FSW joint under micro-galvanic corrosion conditions (a, a_1), and self-corrosion potential versus interface distance curve (b)

zone between AA6016 and AA2519 alloys drives macro-galvanic corrosion; meanwhile, the potential difference between the secondary phase particles in the micro-region away from the interfacial zone and the Al matrix drives micro-galvanic corrosion, jointly leading to the corrosion features shown in Figs. 6(a, a_1−a_6).

Based on the experimental results, the TIG-FSW can effectively enhance the corrosion resistance of the NZ because of two key reasons. Firstly, the dispersed distribution of finer secondary phase particles (Figs. 1(b_1−b_4)) reduces the initiation of pitting corrosion and the intergranular corrosion susceptibility [42]. Secondly, the surface layer only contains AA6016 alloy (Fig. 1(b)). Consequently, there is no significant macro-galvanic corrosion in the NZ, and the corrosion reaction is predominantly triggered by micro-galvanic corrosion between the secondary phase particles and the Al matrix. In the NZ of the TIG-FSW joints, the cathodic and anodic reactions of micro-galvanic corrosion (Fig. 10(a_1)) are similar to those of macro-galvanic corrosion (Fig. 9(a)). In this condition, the Al(Fe,Mn)Si particles have a higher potential and act as the cathode [43], while the Al matrix acts as the anode. As a result, anodic dissolution of the Al matrix occurs, leading to the formation of pitting corrosion, as described schematically in Fig. 10. Therefore, the dispersed distribution of finer secondary phase particles and the uniform microstructure in the NZ of the TIG-FSW joint can contribute to higher corrosion resistance than those of the C-FSW one.

5 Conclusions

(1) TIG-FSW can promote flow, contact and diffusion of the material, reduce the instantaneous cavity, and thus eliminate the tunnel hole defects in the lap joint of AA6016 and AA2519 alloys; moreover, it can reduce the content of oxides inside the joint, eliminate the kissing bond defects, and consequently enhance the tensile properties.

(2) TIG-FSW can eliminate the nonuniform microstructure and promote the formation of a dispersed distribution of finer secondary phase particles, which reduces galvanic corrosion, the initiation of pitting corrosion and intergranular corrosion susceptibility, and finally enhance the corrosion resistance of the NZ.

(3) The tensile strength and elongation of the TIG-FSW joint are (232±3) MPa and (4.8±0.3)%,

respectively, higher than those of (208±1) MPa and (3.2±0.1)% for the C-FSW joint, and the increased rates are about 11.5% and 50.0%, respectively.

(4) The largest corrosion depth and corrosion current density of the NZ in the TIG-FSW joint are 19.4 μm and 1.257 μA/cm^2, respectively, significantly lower than those of 35.7 μm and 5.777 μA/cm^2 for the C-FSW joint, and the reduced rates are about 45.7% and 78.2%, respectively.

CRediT authorship contribution statement

Tie YI: Investigation, Data curation, Writing − Original draft; **Sheng-dan LIU**: Writing − Review & editing; **Chen FANG**: Data curation; **Geng-duo JIANG** and **Xuan-xuan DAI**: Methodology.

Declaration of competing interest

The authors declare that they have no known competing financial interests or personal relationships that could have appeared to influence the work reported in this paper.

Acknowledgments

The authors are grateful to the personnel of National Engineering Research Center of Near-net-shape Forming for Metallic Materials at South China University of Technology and Prof. Da-tong ZHANG for experimental assistance.

References

[1] ÇAM G, JAVAHERI V, HEIDARZADEH A. Advances in FSW and FSSW of dissimilar Al-alloy plates [J]. Journal of Adhesion Science and Technology, 2023, 37: 162−194.

[2] AHMED M M Z, EL-SAYED SELEMAN M M, FYDRYCH D, ÇAM G. Friction stir welding of aluminum in the aerospace industry: The current progress and state-of-the-art review [J]. Materials, 2023, 16: 2971.

[3] KASHAEV N, VENTZKE V, ÇAM G. Prospects of laser beam welding and friction stir welding processes for aluminum airframe structural applications [J]. Journal of Manufacturing Processes, 2018, 36: 571−600.

[4] PATEL V, LI Wen-ya, WANG Guo-qing, WANG Fei-fan, VAIRIS A, NIU Peng-liang. Friction stir welding of dissimilar aluminum alloy combinations: State-of-the-art [J]. Metals, 2019, 9: 270.

[5] CHRISTY J V, MOURAD A H I, SHERIF M M, SHIVAMURTHY B. Review of recent trends in friction stir welding process of aluminum alloys and aluminum metal matrix composites [J]. Transactions of Nonferrous Metals Society of China, 2021, 31: 3281−3309.

[6] LI Yang, MURR L E, MCCLURE J C. Flow visualization and residual microstructures associated with the friction-stir welding of 2024 aluminum to 6061 aluminum [J]. Materials Science and Engineering: A, 1999, 271: 213−223.

[7] BRAUN R, ALFARO MERCADO U A, BIALLAS G. Investigation on strength and corrosion behaviour of friction stir welded similar and dissimilar aluminium alloys [J]. Materials Science Forum, 2006, 519: 1113−1118.

[8] YU Yan, ZHANG Jian-xin, LI Shi-kai. Recent development of friction stir welding for dissimilar materials at home and abroad [J]. Ordnance Material Science and Engineering, 2013, 36: 108−113. (in Chinese)

[9] LI Ying, MURR L E, MCCLURE J C. Solid-state flow visualization in the friction-stir welding of 2024 Al to 6061 Al [J]. Scripta Materialia, 1999, 40: 1041−1046.

[10] MURR L E, LI Ying, FLORES R D, TRILLO E A, MCCLURE J C. Intercalation vortices and related micro-structural features in the friction-stir welding of dissimilar metals [J]. Materials Research Innovations, 1998, 2: 150−163.

[11] ZHANG Ya-li, JIANG Xiao-song, FANG Yan, FANG Yong-jian, LIU Bing, SUN Hong-liang, SHAO Zhen-yi, SONG Ting-feng. Research and development of welding methods and welding mechanism of high-entropy alloys: A review [J]. Materials Today Communications, 2021, 28: 102503.

[12] OUYANG J H, KOVACEVIC R. Material flow and microstructure in the friction stir butt welds of the same and dissimilar aluminum alloys [J]. Journal of Materials Engineering and Performance, 2002, 11: 51−63.

[13] IZADI H, FALLU J, ABDEL-GWAD A, LIYANAGE T, GERLICH A P. Analysis of tool geometry in dissimilar Al alloy friction stir welds using optical microscopy and serial sectioning [J]. Science and Technology of Welding and Joining, 2013, 18: 307−313.

[14] SATYANARAYANA M V N V, KUMAR A, KRANTHI KUMAR K. Towards finding a novel constant between local and bulk strength of friction stir processed aluminum alloys [J]. Proceedings of the Institution of Mechanical Engineers, Part L: Journal of Materials: Design and Applications, 2021, 235: 2151−2164.

[15] SAHA R, BISWAS P. Current status and development of external energy-assisted friction stir welding processes: A review [J]. Welding in the World, 2022, 66: 577−609.

[16] ZENG Jin-cheng, SONG Bo, ZUO Dun-wen, DENG Yong-fang. Research progress of friction stir welding with additional auxiliary conditions [J]. Materials Reports, 2021, 35: 7162−7168. (in Chinese)

[17] BANG H, BANG H, JEON G, OH I, RO C. Gas tungsten arc welding assisted hybrid friction stir welding of dissimilar materials Al6061-T6 aluminum alloy and STS304 stainless steel [J]. Materials & Design, 2012, 37: 48−55.

[18] XU Hui-bin, LUO Lei, ZHANG Shuo, XI Hai-feng. Effect of welding current on interface microstructure of aluminum and steel friction stir welded joints assisted by arc [C]// Proceedings of the 20th Proceedings National Welding Conference. Lanzhou, 2015. (in Chinese)

[19] YI Tie, LIU Sheng-dan, FANG Chen, JIANG Geng-duo. Eliminating hole defects and improving microstructure and mechanical properties of friction stir welded joint of 2519 aluminum alloy via TIG arc [J]. Journal of Materials

Processing Technology, 2022, 310: 117773.

[20] RAJAKUMAR S, MURALIDHARAN C, BALASUBRAMANIAN V. Influence of friction stir welding process and tool parameters on strength properties of AA7075-T6 aluminium alloy joints [J]. Materials & Design, 2011, 32: 535−549.

[21] DU Peng, YAN Xiao-dong, LI Yan-li, SHEN Jian. Transformation mechanism of iron-rich phase in 6061 aluminum alloy during homogenization [J]. The Chinese Journal of Nonferrous Metals, 2011, 21: 981−987. (in Chinese)

[22] HE Hai-lin, YI You-ping, HUANG Shi-quan, ZHANG Yu-xun. Effects of cold predeformation on dissolution of second-phase Al_2Cu particles during solution treatment of 2219 Al−Cu alloy forgings [J]. Materials Characterization, 2018, 135: 18−24.

[23] LI Qing-ming, WEI Xu, DU Bao-shuai, ZHANG Lei. Investigation on the correlation between the selection of polar and heat generation of the anode and cathode during arc welding [J]. Electric Welding Machine, 2011, 41: 29−31. (in Chinese)

[24] CHEN Y C, FENG J C, LIU H J. Precipitate evolution in friction stir welding of 2219-T6 aluminum alloys [J]. Materials Characterization, 2009, 60: 476−481.

[25] RATURI M, BHATTACHARYA A. Mechanical strength and corrosion behavior of dissimilar friction stir welded AA7075−AA2014 joints [J]. Materials Chemistry and Physics, 2021, 262: 124338.

[26] ZHOU Nan, SONG Dong-fu, QI Wen-jun, LI Xiao-hui, ZOU Ji, ATTALLAH M M. Influence of the kissing bond on the mechanical properties and fracture behaviour of AA5083-H112 friction stir welds [J]. Materials Science and Engineering: A, 2018, 719: 12−20.

[27] SATYANARAYANA M, KUMAR A. Influence of cooling media in achieving grain refinement of AA2014 alloy using friction stir processing [J]. Proceedings of the Institution of Mechanical Engineers, Part C: Journal of Mechanical Engineering Science, 2020, 234: 4520−4534.

[28] KADLEC M, RŮŽEK R, NOVÁKOVÁ L. Mechanical behaviour of AA7475 friction stir welds with the kissing bond defect [J]. International Journal of Fatigue, 2015, 74: 7−19.

[29] LIU Hai-bin, WANG Teng-da, LIU Guo-yuan, XIE Shu-feng, CHU Shao-qi, XIE Bin, YANG Sheng-li, WANG Peng-yun. Local microstructure and strengthening mechanisms of double-sided friction stir welded Al−Mg−Mn−Er alloy joint [J]. Transactions of Nonferrous Metals Society of China, 2023, 33: 2588−2598.

[30] YANG Shao-hua, LIU Zeng-wei, LIN Ming, ZHAO Yu-juan, LI Lin-shan. Corrosion behavior of 7075 aluminum alloy in NaCl solutions with different pH values [J]. Nonferrous Metals Science and Engineering, 2017, 8: 7−11. (in Chinese)

[31] MENG Guo-zhe, LI Yang, SHAO Ya-wei, ZHANG Tao, WANG Yan-qiu, WANG Fu-hui, CHENG Xue-qun, DONG Cheng, LI Xiao-gang. Effect of microstructures on corrosion behavior of nickel coatings: (II). Competitive effect of grain size and twins density on corrosion behavior [J]. Journal of Materials Science & Technology, 2016, 32: 465−469.

[32] PENG Yu-chen, HUANG Biao, ZHONG Yue-fang, SU Chang-chao, TAO Zu-shan, RONG Xin-cheng, LI Zhuo-yuan, TANG Hong-qun. Electrochemical corrosion behavior of 6061 Al alloy under high rotating speed submerged friction stir processing [J]. Corrosion Science, 2023, 215: 111029.

[33] SATYANARAYANA M V N V, MANOHAR G, JAIN V K S, KUMAR K K, KUMAR A, SUNDAR S. Influence of cooling media on the electrochemical behavior of friction stir processed Al2014 alloy [J]. JOM, 2023, 75: 526−536.

[34] ASTARITA A, BITONDO C, SQUILLACE A, ARMENTANI E, BELLUCCI F. Stress corrosion cracking behaviour of conventional and innovative aluminium alloys for aeronautic applications [J]. Surface and Interface Analysis, 2013, 45: 1610−1618.

[35] ANIL KUMAR H M, VENKATA RAMANA V. Influence of tool parameters on the tensile properties of friction stir welded aluminium 5083 and 6082 alloys [J]. Materials Today: Proceedings, 2020, 27: 951−957.

[36] MA He, WANG Yue, TIAN Zhi-jie, XIONG Lin-yu, ZHANG Yan-hua. Gap-tolerance control for friction stir butt welding of 2A14 aluminium alloy [J]. Measurement, 2019, 148: 106915.

[37] ZHANG Cheng-hang, HUANG Guang-jie, CAO Yu, ZHU Yu-long, LI Wei, WANG Xiao-dong, LIU Qing. Microstructure and mechanical properties of dissimilar friction stir welded AA2024-7075 joints: Influence of joining material direction [J]. Materials Science and Engineering: A, 2019, 766: 138368.

[38] SATO Y S, URATA M, KOKAWA H. Parameters controlling microstructure and hardness during friction-stir welding of precipitation-hardenable aluminum alloy 6063 [J]. Metallurgical and Materials Transactions A, 2002, 33: 625−635.

[39] DELRUE S, TABATABAEIPOUR M, HETTLER J, VAN DEN ABEELE K. Applying a nonlinear, pitch-catch, ultrasonic technique for the detection of kissing bonds in friction stir welds [J]. Ultrasonics, 2016, 68: 71−79.

[40] VIKAS K S R, RAMANA V V, MOHAMMED R, REDDY G M, RAO K. Influence of post weld heat treatment on microstructure and pitting corrosion behavior of dissimilar aluminium alloy friction stir welds [J]. Materials Today: Proceedings, 2019, 15: 109−118.

[41] ZHANG Xian-man, CHEN Zai-yu, LUO Hong-feng, ZHOU Teng, ZHAO Yu-liang, LING Zi-cheng. Corrosion resistances of metallic materials in environments containing chloride ions: A review [J]. Transactions of Nonferrous Metals Society of China, 2022, 32: 377−410.

[42] SATYANARAYANA M V N V, KUMAR A, THAPLIYAL S. Effect of microstructure and precipitate formation on mechanical and corrosion behavior of friction stir processed AA6061 alloy using different cooling media [J]. Proceedings of the Institution of Mechanical Engineers, Part L: Journal of Materials: Design and Applications, 2021, 235: 2454−2469.

[43] ALLACHI H, CHAOUKET F, DRAOUI K. Protection against corrosion in marine environments of AA6060 aluminium alloy by cerium chlorides [J]. Journal of Alloys and Compounds, 2010, 491: 223−229.

TIG 氩弧改善 AA6016 和 AA2519 铝合金搅拌摩擦焊搭接接头的显微组织、拉伸性能和耐蚀性能

易 铁[1,2,3]，刘胜胆[1,2,3]，方 晨[1,3]，江耿铎[4]，戴轩轩[1,3]

1. 中南大学 材料科学与工程学院，长沙 410083；
2. 中南大学 轻质高强结构材料国家级重点实验室，长沙 410083；
3. 中南大学 有色金属材料科学与工程教育部重点实验室，长沙 410083；
4. 华南理工大学 机械与汽车工程学院，广州 510640

摘 要：采用光学显微镜、扫描电子显微镜、室温拉伸试验、腐蚀浸泡试验和电化学测试等方法，研究了 TIG 氩弧辅助搅拌摩擦焊接（TIG-FSW）对 AA6016 和 AA2519 铝合金搭接接头显微组织、拉伸性能和耐蚀性能的影响。结果表明，在 FSW 过程中引入 TIG 氩弧后，接头的显微组织更加均匀，且不存在隧道孔缺陷。此外，它提高了接头的抗拉强度和伸长率，提高率分别为 11.5%和 50.0%；同时，降低了腐蚀电流密度和最大腐蚀深度，降低率分别为 78.2%和 45.7%。TIG-FSW 能促进材料的流动、接触和扩散，从而改善接头的显微组织。另外，它还使第二相粒子的尺寸减小、数量减少。因此，这些因素有助于提高接头的拉伸性能和耐蚀性能。

关键词：搅拌摩擦焊接；搭接接头；异种铝合金；第二相颗粒；显微组织；拉伸性能；耐蚀性能

(Edited by Wei-ping CHEN)